



Study on the flow and heat transfer performance of nanofluid in a novel manifold microchannel heat sink combining trapezoidal cross-section and curved corners

Zhiguo Tang¹ · Ran Sun¹ · Kuan Lu¹ · Jianping Cheng¹ · Pei Zhou²

Received: 2 February 2024 / Accepted: 26 April 2024 / Published online: 18 May 2024
© Akadémiai Kiadó, Budapest, Hungary 2024

Abstract

The manifold microchannel heat sink (MMCHS) has been widely used in the field of electronic device cooling due to its high heat dissipation ability. In order to further reduce the flow resistance and improve the heat transfer performance of the microchannel, this paper proposes a novel MMCHS combining trapezoidal cross-section and curved corners and referred to as TC-MMCHS. Al₂O₃-water nanofluid was used as the coolant. The impacts of the channel cross-sectional shapes, curved corners, trapezoidal structure parameters, and nanoparticle volume fraction on the flow and heat transfer performance of MMCHS were numerically studied. The results showed that, for the same pumping power, compared with the four MMCHS structures, the trapezoidal flat MMCHS (TF-MMCHS) has the lowest thermal resistance and entropy generation, and therefore it exhibits the highest overall performance. The introduction of curved corners significantly reduces the flow resistance, and compared with TF-MMCHS, the pumping power of TC-MMCHS decreases by up to 11.33%. When the bottom angle is equal to 78.7°, the heat transfer characteristics and irreversible losses of TC-MMCHS reach their optimal values. The increase of the channel width is not conducive to the improvement of heat transfer characteristics. However, it can significantly decrease the pumping power by 69.85%. Compared with the conventional MMCHS which uses deionized water as coolant, the introduction of Al₂O₃-water nanofluid into TC-MMCHS reduces the thermal resistance and entropy generation by 14.22% and 12.36%, respectively. This significantly improves its heat transfer characteristics and reduces irreversible losses.

Keywords Manifold microchannel heat sink · Numerical simulation · Trapezoidal cross-section · Curved corner · Nanofluid

List of symbols

Abbreviations

<i>A</i>	The heated surface area (m ²)
<i>c_p</i>	Specific heat capacity (J kg ⁻¹ K ⁻¹)
<i>D</i>	Hydraulic diameter (μm)
<i>d</i>	Diameter (μm)
<i>H</i>	Height (μm)
<i>H_S</i>	Height of the base (μm)
<i>h</i>	Enthalpy
<i>k</i>	Thermal conductivity (W m ⁻¹ K ⁻¹)

<i>L</i>	Length (μm)
<i>M</i>	Molecular mass of water (g mol ⁻¹)
<i>m</i>	Total mass flow rate (kg s ⁻¹)
<i>O</i>	Avogadro constant
<i>P</i>	Pressure (Pa)
<i>P_p</i>	Pumping power (W)
<i>Q</i>	Total heat flux (W)
<i>q</i>	Heat flux (W cm ⁻²)
<i>R_t</i>	Thermal resistance (K W ⁻¹)
Re	Reynolds number
<i>r</i>	Radii of the curved corners (μm)
<i>S_{gen}</i>	Total entropy generation (W K ⁻¹)
<i>s</i>	Entropy (W K ⁻¹)
<i>T</i>	Temperature (K)
<i>T_{bm}</i>	The maximum temperature of substrate (K)
<i>u</i>	Velocity (m s ⁻¹)
<i>V</i>	Total volume flow rate (m ³ s ⁻¹)
<i>W</i>	Width (μm)

✉ Jianping Cheng
chjianping@hfut.edu.cn

✉ Pei Zhou
zhoupei@hfut.edu.cn

¹ School of Mechanical Engineering, Hefei University of Technology, Hefei 230009, Anhui, China

² School of Automotive and Transportation Engineering, Hefei University of Technology, Hefei 230009, Anhui, China

Greek letters

α	Bottom angle of the trapezoid ($^{\circ}$)
ρ	Density (kg m^{-3})
μ	Dynamic viscosity (Pa s)
φ	Volume fraction of nanoparticles

Subscripts

a	Top of channel
b	Bottom of channel
c	Trapezoidal channel
f	Fin
l	Fluid
m	Manifold
s	Solid
bl	Basic fluid
in	Inlet
nl	Nanofluid
np	Nanoparticle
out	Outlet

Introduction

The continuous development of electronic devices toward miniaturization, high power, and integration improved their performance. However, this caused a significant growth in their heat flow density [1, 2]. If the heat of the electronic devices cannot be dissipated in a timely and effective manner, it will reduce their operational stability and service life, and it can lead to burning in serious cases. Traditional cooling techniques, such as natural convection and forced air cooling, are powerless for electronic devices with local hotspots reaching 1000 W cm^{-2} [3]. To assure the normal functioning of electronic equipment, many studies proposed a series of efficient cooling technologies including heat pipes [4], jet impingement [5, 6], boiling phase change [7, 8], and microchannel heat sink [9, 10]. Among them, the

microchannel cooling technology has been widely studied and applied due to its outstanding reliability and cooling properties [10].

The thermal management technique of microchannel heat sinks (MCHS) was first introduced by Tuckerman and Pease [11]. They deduced that the MCHS can remove heat flow density of up to 790 W cm^{-2} . However, it also causes high pressure loss reaching 241 kPa. Afterward, in order to obtain high cooling performance under low pressure drop conditions, many researchers performed various optimized designs of MCHS structure, such as cavities [12, 13], ribs [14, 15], secondary channels [16, 17], wave channels [18, 19], and channel cross-section shape variations [20, 21], as shown in Table 1. Zhai et al. [13] deduced that the fan-shaped cavities can maintain low pressure loss and improve the flow characteristics in the channel. Zhu et al. [14] introduced different shapes of ribs based on fan-shaped cavities and achieved the highest performance by combining them. Kuppusamy et al. [16] proposed a design approach for secondary oblique channels, which, respectively, reduces the thermal resistance by 76.8% compared with the traditional MCHS, and improves the overall performance by 146%. Zhang et al. [20] designed three types of microchannels having the same cross-section but different shapes (rectangle, trapezoid, and circle). When the inlet flow rate is the same, they deduced that trapezoid microchannel has the optimum cooling ability, while the circular channel has the highest pumping power. Although the structural optimization of MCHS can improve its cooling performance, it is essentially achieved by breaking the development of boundary layers during the flow process, which intensifies the fluid disturbances and thus enhances the heat dissipation capacity of MCHS. The problem of large temperature difference between the entrance-export and high energy losses caused by the long flow process of the coolant in the MCHS has not been completely solved.

Table 1 Classification of the microchannel enhanced heat transfer methods

Type	Structural optimization	Coolant	Conclusion	References
MCHS	MCHS	Water	Capable of removing heat flux density up to 790 W cm^{-2}	[11]
	MCHS with fan-shaped cavities	Water	The fan-shaped cavity can maintain a low-pressure drop	[14]
	MCHS with secondary channels	Water	Compared to traditional MCHS, the overall performance of secondary channel has improved by 146%	[16]
	Channel cross-section shapes	Water	The trapezoidal channel has the best cooling performance	[20]
MMCHS	MMCHS	Water	Reduced pressure drop due to shortened channel length	[22]
	Manifold arrangements	HFE-7100	H-type and U-type arrangements reduce pressure drop	[24]
	Manifold structure shapes	Water	Parabolic manifolds exhibit the best overall performance	[25]
	Open MMCHS	Water	Reduced pressure drop due to the elimination of channel walls at the inlet and outlet	[27]
	MMCHS with corrugated bottom	CuO-water nanofluid	Compared with traditional MMCHS, both pressure drop and thermal resistance are significantly reduced	[29]

To solve the aforementioned problems in the MCHS, Harpole and Eninger [22] first proposed the concept of manifold microchannel heat sink (MMCHS). They used manifolds with alternating inlet–outlet distributions to evenly distribute the coolant into the microchannels, which drastically shortened the flow path of coolant, leading to a remarkable reduction in power consumption and thermal resistance. Afterward, there has been a proliferation of researches on the flow and heat transfer characteristics of MMCHS [23–29]. Most of these studies focus on the following two aspects.

On the one hand, some studies tackle the arrangement and structural types of the upper manifold. For instance, in the design of manifold arrangement, Luo et al. [23] found that the traditional Z-type arrangement has lower flow uniformity and heat transfer performance compared with the H-type and U-type arrangements. Lin et al. [24] designed HU-type and ZU-type arrangements to further decrease the pumping power. They deduced that these arrangements decrease the pressure loss of the MMCHS and increase its temperature uniformity. Chen et al. [25] also deduced that compared with the conventional rectangular manifold, the conical manifold has lower pressure drop, while the parabolic manifold has the highest comprehensive performance.

On the other hand, there are mostly existing researches focusing on the optimization of the bottom microchannel structure. Mandel et al. [26] used a 2.5-D approach to demonstrate that the fluid causes significant pressure loss when passing through sharp turns in the MMCHS. It is evident from the MMCHS that sharp turns are mainly caused by the contraction and expansion of the inlet–outlet of microchannel as well as its corners. Many studies performed optimized designs for the microchannel structure to reduce the pressure loss caused by sharp turns while maintaining low thermal resistance. For instance, Gilmore et al. [27] proposed an open MMCHS structure that reduces the pressure drop by 25% by eliminating microchannel walls at the inlet and outlet. Tang et al. [28] designed the novel MMCHS with divergent/convergent channels. They found that for the same pumping power, the thermal resistance of new structure is reduced by 19.18% compared with the traditional rectangular channel. Cheng et al. [29] introduced the novel MMCHS with corrugated bottom surface for optimizing the bottom corner of the microchannel. Their results showed that the pumping power and thermal resistance were, respectively, reduced by 43.81% and 14.86% compared with the MMCHS of flat bottom surface.

It can be deduced from this literature review that the optimization of the inlet–outlet cross section of the microchannel and the channel corners in MMCHS significantly affects the reduction of the thermal resistance and pumping power.

In recent years, the widespread adoption of nanofluids technology has made it possible to enhance heat transfer by adding solid particles to coolants [30, 31]. Compared with

traditional coolants, nanofluids have higher heat transfer coefficient. Therefore, many researchers introduced them into the field of microchannels to achieve a better cooling effect [32, 33]. Most of the studies on nanofluids focused on the size [34], type [35], volume fraction [36], and flow state of the nanoparticles [37, 38]. Yue et al. [34] studied the effects of nanoparticles with different diameters on the flow and thermal properties of the MMCHS. They deduced that, when the particle diameter increases, the Nusselt number and pumping power decrease, while the entropy generation increases. Alfaryjat et al. [35] studied the impacts of four nanofluids on the hydraulic and thermal properties of the MCHS. They deduced that for the same friction coefficient, the Al_2O_3 –water nanofluid has the highest heat transfer coefficient. Pourfattah et al. [36] found that the heat transfer performance of MMCHS is improved with the increase of the concentration of CuO–water nanofluids at the expense of increasing the pumping power. Moreover, the comprehensive performance reaches the highest value for a concentration of nanoparticles of 2%.

It can be deduced from the above literature review that MMCHS has higher cooling characteristics and lower pressure loss than MCHS. However, most of the studies on the MMCHS are based on conventional rectangular channel while not taking into consideration the optimization of the channel types. The variation of channel cross section in the MCHS has been widely studied and has demonstrated excellent potential in improving the thermal properties [20, 21]. In addition, relevant studies confirmed that curved corners in channels have better flow characteristics than rectangular corners [39, 40]. In order to further enhance the heat transfer characteristics and decrease the pressure loss of MMCHS, this paper proposes four-channel cross-section shapes of the MMCHS, along with the introduction of curved corner structure. The Al_2O_3 –water nanofluid was used as the coolant. The thermal resistance, pumping power, and entropy generation were used as the performance evaluation indexes. The impacts of channel cross-sectional shapes, size of curved corners, and nanofluid parameters on the flow and heat transfer performance of the MMCHS were finally studied.

Physical model and numerical methods

Physical model

Figure 1a illustrates the novel MMCHS structure combining trapezoidal cross-section channel and curved corners and referred to as TC-MMCHS. The heat flux enters the TC-MMCHS from the substrate. The coolant enters the inlet manifold channel and then flows through the bottom trapezoidal channel, removing heat from the heated wall

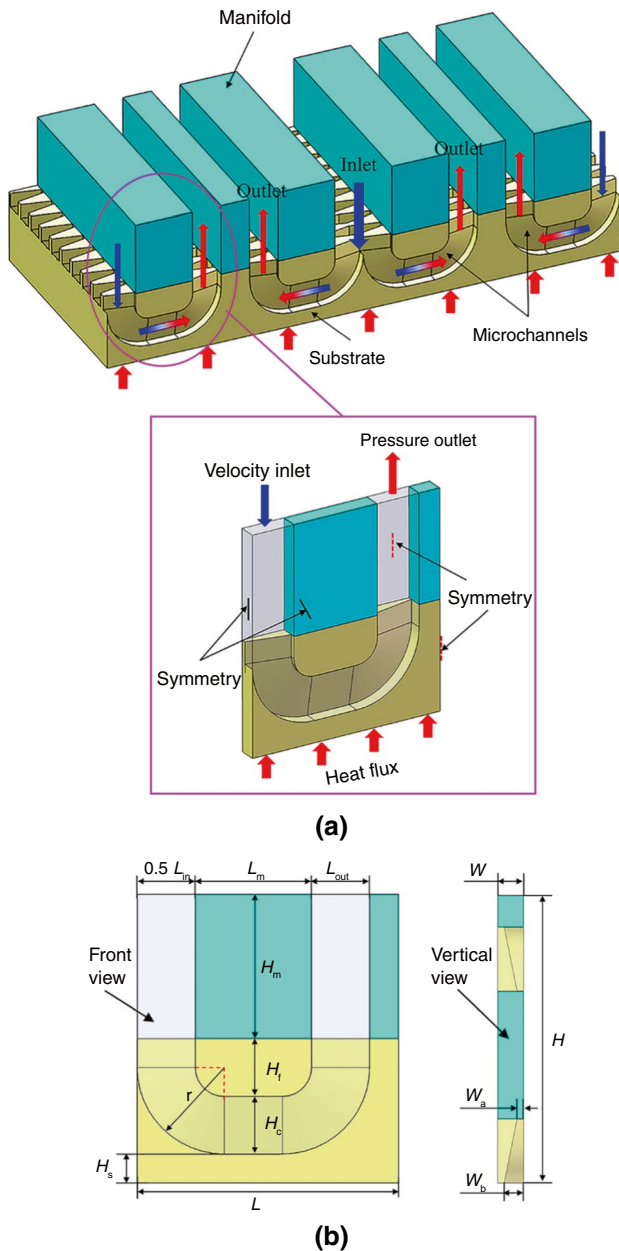


Fig. 1 **a** Schematic of the MMCHS with trapezoidal cross-section and curved corners, **b** structural parameters of the calculation model

surface through convective heat exchange. It finally flows out through the adjacent outlet manifold channel.

Due to the symmetry of the TC-MMCHS, the simplified physical model includes half an inlet manifold channel, a trapezoidal cross-section channel, and a complete outlet manifold channel, as shown in the purple wireframe in Fig. 1a. The geometric parameters of the computational domain model are shown in Fig. 1b, where L , W , and H , respectively, represent the length, width, and height of the entire computational domain model, L_{in} is the inlet length

Table 2 Structural parameters in the calculation domain

Parameters	Description	Value/ μm
L	Length of model	450
L_{in}	Length of inlet	200
L_{out}	Length of outlet	100
L_m	Length of manifold	200
W	Width of model	40
W_a	Top width of trapezoid channel	10
W_b	Bottom width of trapezoid channel	30
H	Height of model	500
H_m	Height of manifold	250
H_f	Height of fin	100
H_c	Height of trapezoid channel	100
H_s	Height of the base	50
r	Radii of the curved corners	150

of manifold channel, L_m is the manifold length, W_a and W_b , respectively, denote the upper and bottom widths of the trapezoidal cross section, H_m is the manifold height, H_f , H_c , and H_s , respectively, represent the height of fin, channel, and substrate. r represents the radii of the curved corner. Table 2 displays the detailed structural parameters of the calculation domain.

Governing equations

The following assumptions were introduced to streamline the calculation process for the numerical model:

- (1) The flow of the fluid is stable, laminar, and incompressible.
- (2) Thermophysical properties of the solid materials are constant.
- (3) Viscous dissipation effects and environmental heat losses are neglected.

Based on these assumptions, the control equations for flow and thermal transfer in TC-MMCHS under single-phase flow can be expressed as:

Continuity equation:

$$\frac{\partial}{\partial x_i} (\rho u_i) = 0 \quad (1)$$

Momentum equation:

$$\frac{\partial}{\partial x_j} (\rho u_i u_j) = -\frac{\partial p}{\partial x_i} + \frac{\partial}{\partial x_j} \left(\mu_{nl} \frac{\partial u_i}{\partial x_j} \right) \quad (2)$$

Energy equation of the fluid and solid:

$$\frac{\partial}{\partial x_j} (\rho u_j c_p T_1) = \frac{\partial}{\partial x_j} \left(k_1 \frac{\partial T_1}{\partial x_j} \right) \tag{3}$$

$$\frac{\partial}{\partial x_j} \left(k_s \frac{\partial T_s}{\partial x_j} \right) = 0 \tag{4}$$

where ρ represents the density, u is the flow rate, μ_l and c_p , respectively, denote the viscosity and specific heat capacity, p , k and T , respectively, represent the pressure, heat conductivity and temperature, the subscripts l and s represent the fluid and solid, respectively.

Nanofluid properties

The thermophysical parameters of the equivalent single-phase flow of Al₂O₃-water nanofluid can be deduced from the corresponding expressions:

Density and specific heat capacity [35]:

$$\rho_{nl} = (1 - \varphi)\rho_{bl} + \varphi\rho_{np} \tag{5}$$

$$c_{p,nl} = \frac{(1 - \varphi)\rho_{bl}c_{p,bl} + \varphi\rho_{np}c_{p,np}}{\rho_{nl}} \tag{6}$$

Thermal conductivity [41]:

$$k_{nl} = k_{bl} \left(\frac{2k_{bl} + k_{np} + 2\varphi(k_{np} - k_{bl})}{2k_{bl} + k_{np} - \varphi(k_{np} - k_{bl})} \right) \tag{7}$$

Dynamic viscosity [42]:

$$\mu_{nl} = \mu_{bl} \left(1 + 49.6 \times \left(\frac{d_{np}}{d_{bl}} \right)^{-0.414} \varphi^{0.908} e^{10.8\varphi} \right) \tag{8}$$

$$d_{bl} = 0.1 \left(\frac{6M}{O\pi\rho_{bl}} \right)^{1/3} \tag{9}$$

where φ represents the volume fraction of nanoparticles, nl, bl, and np, respectively, represent the nanofluid, basic fluid, and nanoparticle, d_{bl} is the diameter of Al₂O₃ nanoparticles, M is the molecular mass of water, and O represents the Avogadro constant (6.022×10^{23}).

Table 3 presents the thermophysical parameters of water and aluminum oxide at 293 K.

Boundary conditions

The material of the heat sink is made of silicon ($\rho_s = 2330 \text{ kg m}^{-3}$, $c_{p,s} = 712 \text{ J kg}^{-1} \text{ K}^{-1}$, $k_s = 148 \text{ W m}^{-1} \text{ K}^{-1}$). A constant heat flow density (q) of 400 W cm^{-2} is set on the

Table 3 Parameters of nanofluid nanoparticles and water

Material	$c_p/\text{J kg}^{-1} \text{ K}^{-1}$	$\rho/\text{kg m}^{-3}$	$k/\text{W m}^{-1} \text{ K}^{-1}$	$\mu/\text{Pa s}$
Al ₂ O ₃	773	3880	36	–
Water	4182	998.2	0.597	9.93×10^{-4}

bottom of microchannel. The inlet and outlet of coolant are set equal to the velocity inlet and pressure outlet, respectively. The front, back, right, and left sides of the calculation model were set as symmetry surfaces with a gradient of null. The inner faces are set as non-slip walls, and the other faces are set as adiabatic walls. The coupling surface of the fluid and solid is set as a conjugate heat transfer surface to achieve the continuity of heat flow density.

During the numerical simulation process, the governing equations are discretized by using finite volume method, followed by iterative solutions. The fluid flow equation is then solved by coupling the pressure and velocity using the SIMPLEC algorithm. In addition, it is recognized that the numerical calculation converges (i.e., the calculation is stopped) when the residual values of energy and continuity equations are below 10^{-9} and 10^{-6} , respectively.

Parameter definition

The parameters used to study the flow and thermal performance of MMCHS are given by:

(1) Reynolds number:

$$Re = \frac{\rho_{nl} u_{in} D}{\mu_{nl}} \tag{10}$$

where D is the hydraulic diameter.

(2) Total thermal resistance of the MMCHS:

$$R_t = \frac{T_{bm} - T_{in}}{Q} \tag{11}$$

$$Q = q \times A \tag{12}$$

where T_{bm} represents the maximum temperature of substrate, T_{in} denotes the inlet temperature of nanofluid, Q denotes the total heat flow, and A represents the total heated area of the entire radiator.

(3) (3) The total pump work is computed as:

$$P_p = V \times \Delta P \tag{13}$$

where V is the total volume flow rate, ΔP represents the pressure drop of the fluid.

(4) The total entropy generation (S_{gen}) is commonly applied to analyze irreversible losses in flow and heat transfer

processes. It is primarily composed of thermal and friction entropy generation. Therefore, the use of S_{gen} as evaluation index allows to analyze the effects on the overall performance of MMCHS [43].

The general expression for entropy generation can be determined by the second law of thermodynamics:

$$\frac{dS_{sys}}{dt} = m(s_{in} - s_{out}) + \frac{Q}{T_{bm}} + S_{gen} \tag{14}$$

where s_{in} and s_{out} represent the entropy flowing into and out of MMCHS, respectively. m represents the total mass flow rate.

Based on the steady-state assumption, it can be inferred that dS_{sys}/dt is null, and therefore:

$$h_{out} - h_{in} = T_{in}(s_{out} - s_{in}) + \frac{\Delta P}{\rho} \tag{15}$$

$$Q = m(h_{out} - h_{in}) \tag{16}$$

Thus, the expression of total entropy generation is:

$$S_{gen} = \frac{Q(T_{bm} - T_{in})}{T_{bm}T_{in}} + \frac{m\Delta P}{\rho T_{in}} \tag{17}$$

Grid independence verification

Grid independence validation is performed to ensure the high accuracy and reliability of the numerical calculation results. The division of overall grid and near wall grid of MMCHS is shown in Fig. 2. The solid domain grid adopts a tetrahedral mesh, while the fluid domain grid adopts a structured hexahedral mesh and is locally refined. Figure 3 displays the effect of grid number on R_t and P_p . When the

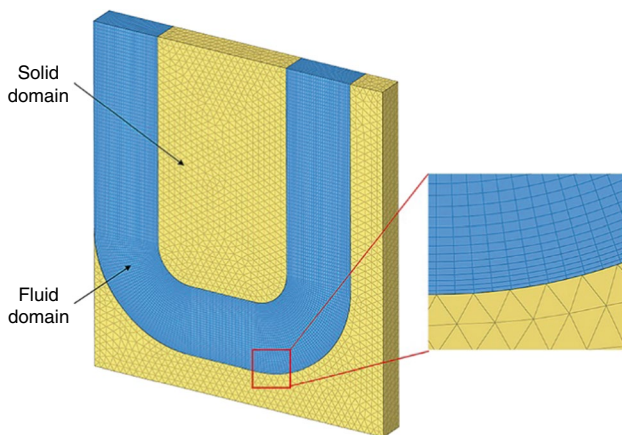


Fig. 2 Schematic of the grid model

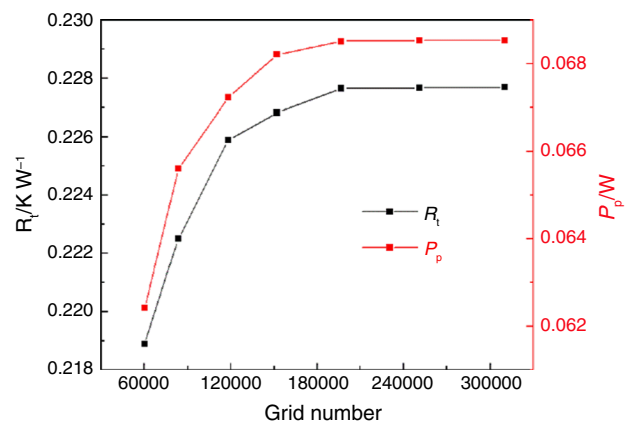


Fig. 3 Grid independence verification

grid number increases to 196,780, R_t reaches 0.2277 K W^{-1} , and P_p reaches 0.0685 W . As the grid continues to refine, the changes in R_t and P_p tend to stabilize. Therefore, a grid size corresponding to the grid number of 196,780 is adopted as the standard for the subsequent computational model meshing, which ensures the high accuracy of the computational results and reduces calculation time.

Model validation

In order to verify the accuracy of the adopted numerical calculation method, its results are compared with the experimental results of Drummond et al. [44]. HFE-7100 is used as the refrigerant, and the heat flux density at the bottom of radiator is set in the range of $0\text{--}120 \text{ W cm}^{-2}$. The comparison between the experimental and simulation data for the average temperature of heated surface at different heat flux densities is illustrated in Fig. 4. It can be seen that the maximum difference between the simulation and experimental

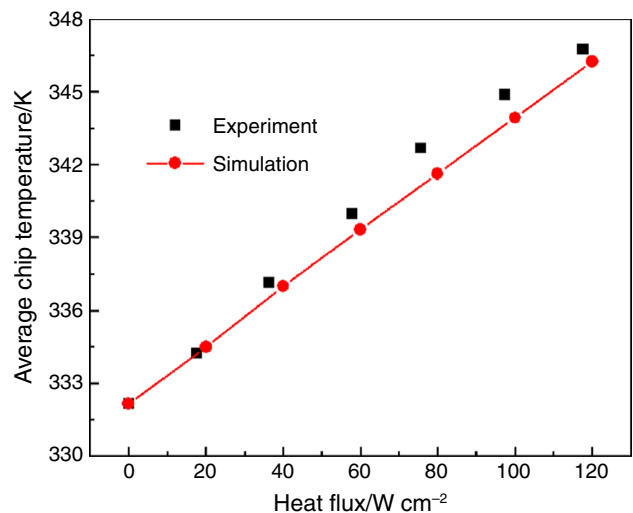


Fig. 4 Validation of the numerical simulation

data is less than 1.1 K, and the error is within 0.5%. Therefore, the simulation method adopted in this paper is feasible.

Results and discussion

Effect of different channel cross-section shapes

In this paper, four structural design schemes are proposed to investigate the influence of different channel cross-section shapes on the flow and thermal performance of flat MMCHS (F-MMCHS) (Fig. 5): rectangular flat MMCHS

(RF-MMCHS), trapezoidal flat MMCHS (TF-MMCHS), inverted trapezoidal flat MMCHS (ITF-MMCHS), and half ellipsoidal flat MMCHS (HEF-MMCHS). The cross-sectional area of the channel remains constant across all the design schemes, measuring $40\ \mu\text{m} \times 100\ \mu\text{m}$. The volume fraction of the Al_2O_3 -water nanofluid is 2%.

Hydrodynamic performance

Figure 6b exhibits the change of P_p with Re for four structures of F-MMCHS. When the Re of the nanofluid increases, the P_p of all the four F-MMCHSs increases and the addition

Fig. 5 Schematic of the F-MMCHS with four different structures

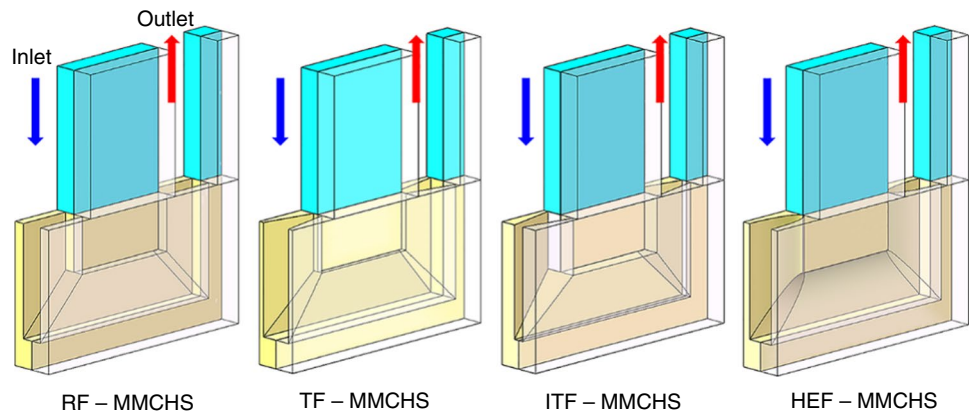
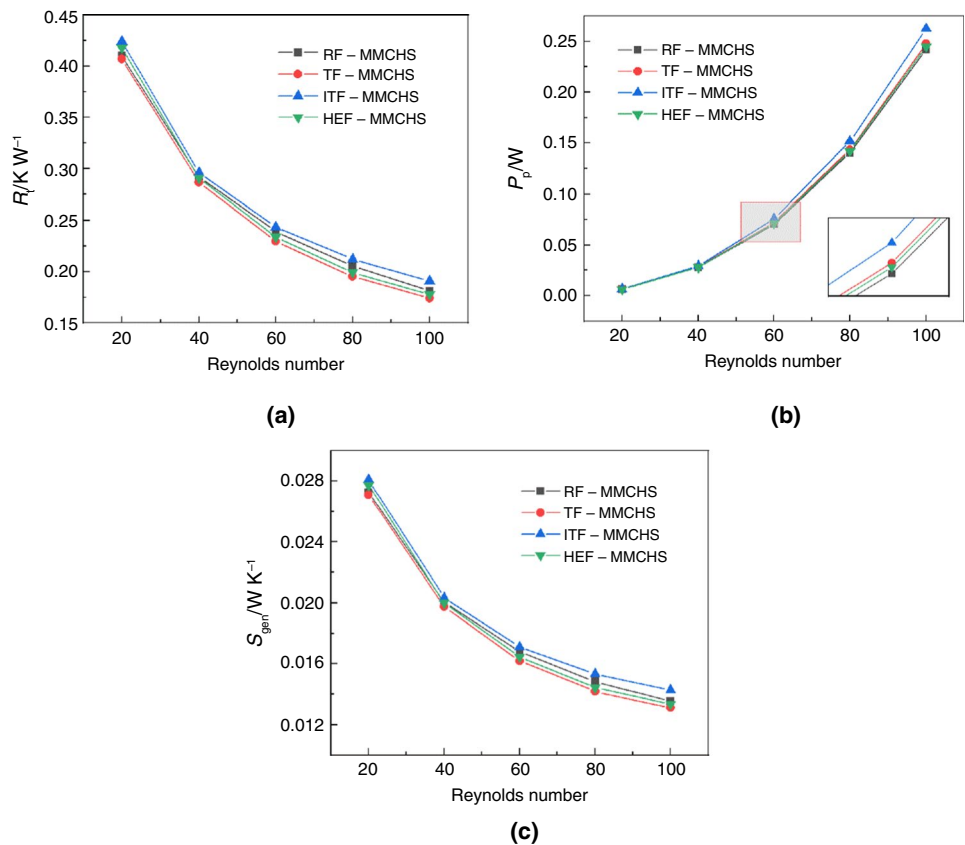


Fig. 6 Variation of the performance parameters of F-MMCHS with four different structures function of Re: **a** R_t , **b** P_p , and **c** S_{gen}

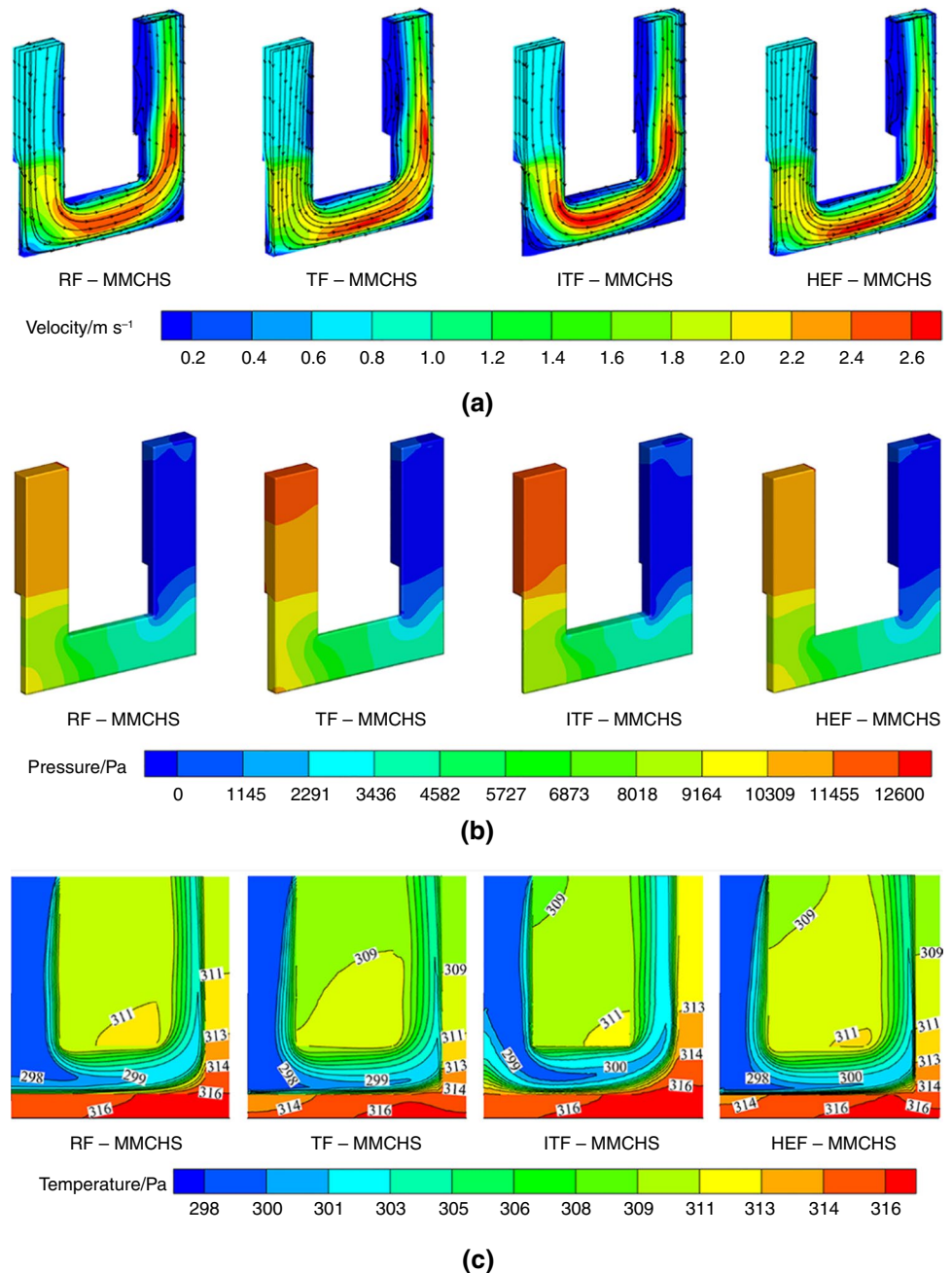


becomes progressively larger. For the same Re of 60, the P_p of the ITF-MMCHS is maximum (0.076 W) and that of the RT-MMCHS is minimum (0.070 W). Figure 7b illustrates that ITF-MMCHS has the highest pressure, followed by TF-MMCHS, while HEF-MMCHS and RT-MMCHS have significantly lower pressures. The high-pressure areas are mainly concentrated at the inlet and bottom corners of the channel.

From Fig. 7a, it is evident that when the nanofluid flows from the upper manifold to bottom microchannel, due to the contraction of the channel cross-section area, the fluid undergoes a gathering phenomenon and the flow velocity

rapidly increases. This results in increasing pressure at the inlet [27]. Compared to TF-MMCHS and HEF-MMCHS, RT-MMCHS and ITF-MMCHS have higher pressure at the inlet. The significant pressure variation at the bottom corner of the microchannel is mainly due to the sudden change in the flow direction when coolant flows through the microchannel, resulting in an increase of the pressure. Compared to the other three structural channels of F-MMCHSs, the overall uniformity of the flow velocity in the ITF-MMCHS is significantly lower. This is mainly because there are large flow stagnation zones at the corners on the two sides of the bottom of the channel, which

Fig. 7 F-MMCHS contour maps with four different structures at Re of 60: **a** velocity, **b** pressure, and **c** temperature



results in extremely low flow velocity and maximum pressure loss.

Meanwhile, it can be clearly seen from Fig. 8 that compared to rectangular channel, the narrow upper and wide lower structures of trapezoidal and half ellipsoidal channels force more coolant to flow through their lower half, resulting in a high flow velocity region at the bottom of the channel. For inverted trapezoidal channel, the flow velocity of the coolant in the middle part of the channel is higher.

Heat transfer performance

Figure 6a demonstrates the relationship between the heat transfer performance and Re for the F-MMCHSs with different structural designs. It is evident that with an increase of Re from 20 to 100, the R_t of the four F-MMCHSs gradually decreases and the heat transfer performance is improved. This is due to the fact that the increase in Re makes the impact strength between the coolant and the wall increase, hindering the development of the thermal boundary layer and enhancing its cooling effect. However, the rate of decrease of R_t becomes smaller with increasing

Re . For the same Re , the R_t of the four F-MMCHSs always exhibits the following descending order: TF-MMCHS, HEF-MMCHS, RF-MMCHS, and ITF-MMCHS.

Figure 7c illustrates the temperature contour maps of F-MMCHSs at Re of 60. Compared with RF-MMCHS, TF-MMCHS and HEF-MMCHS have higher cooling properties, while that of ITF-MMCHS is deteriorated. This is because the heat flux is set at the bottom of the heat sink, so the larger width at the bottom of the microchannel means the larger heat transfer area facing the heat flow side, which is beneficial to enhance cooling performance. The bottom width of the trapezoidal and half ellipsoidal microchannels is larger than that of the rectangular microchannel, which improves its cooling properties, while the opposite holds for the inverted trapezoidal microchannel. This phenomenon indicates that the width of the bottom of the microchannel significantly enhances the cooling effect [45]. In addition, it is affected by the distribution of coolant flow. It is evident from Figs. 7a and 8 that, compared to the rectangular channel, the narrow upper and wide lower structures of the trapezoidal and half ellipsoidal channels force more coolant to flow through their lower half, which promotes the heat transfer. In contrast, the inverted trapezoidal channel makes the coolant flow through the middle part of the channel, which reduces its cooling capacity.

Considering the optimization objective of the MMCHS (i.e., ensuring that the temperature of the electronic devices is within the normal working range while consuming less power), the variation of R_t with P_p in F-MMCHSs is further analyzed, as shown in Fig. 9a. When P_p increases, the R_t of the four F-MMCHSs shows a gradually decreasing trend. However, the magnitude of the decrease is gradually reduced. For the same P_p value, the R_t of ITF-MMCHS is the largest, followed by those of RF-MMCHS and HEF-MMCHS, while TF-MMCHS has the smallest R_t , and therefore its heat transfer capacity is the highest.

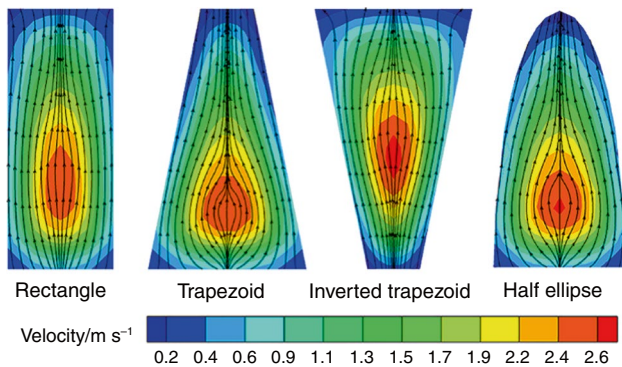
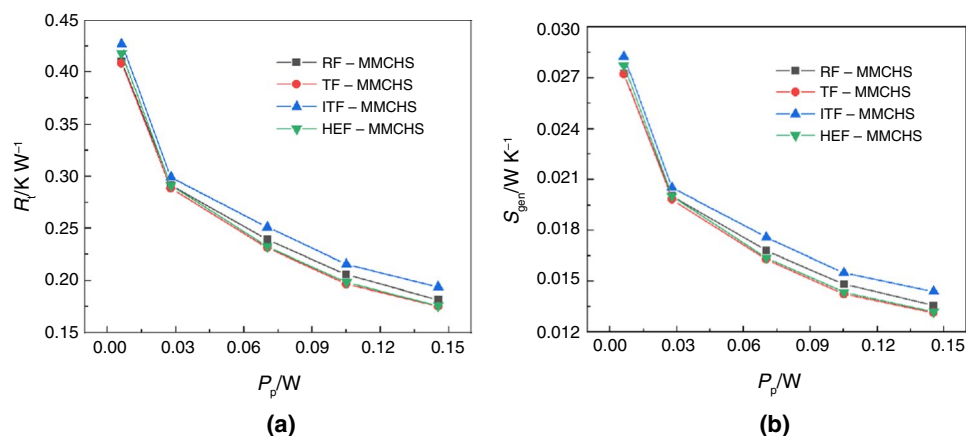


Fig. 8 Velocity contours and streamlines at the middle section of the four channels

Fig. 9 Variation of **a** R_t and **b** S_{gen} with P_p for four structures of F-MMCHS



Total entropy generation

From Fig. 6c, when Re increases, the S_{gen} of the four F-MMCHSs gradually decreases. S_{gen} denotes the sum of heat transfer entropy generation and friction entropy generation, while its trend is consistent with the change of R_t and opposite to that of P_p , which suggests that the heat transfer entropy generation takes the major role in this case [46]. The S_{gen} of TF-MMCHS is the smallest one, and thus it has better flow and heat transfer irreversibility. As previously mentioned, the cooling performance of ITF-MMCHS is the worst, and the pumping power consumption is also the highest. Therefore, it has the largest heat transfer entropy generation and friction entropy generation. This results in the highest total entropy generation, which causes higher irreversible energy losses.

When P_p increases, the S_{gen} of the four F-MMCHSs shows a gradually decreasing trend (Fig. 9b), being consistent with the decreasing trend of R_t . This is mainly due to the fact that, when P_p is constant, the friction entropy generation remains unchanged, and the changes in S_{gen} are only related to the thermal performance. Therefore, for the same P_p value, the irreversible energy losses of MMCHS with four-channel shapes, from high to low, are as follows: ITF-MMCHS, RF-MMCHS, HEF-MMCHS, and TF-MMCHS. As a result, the TF-MMCHS has optimal hydraulic and thermal properties (Fig. 10).

Effect of the radii of the curved corners in the microchannel

Curved structures are introduced into the corners of the channel (i.e., TC-MMCHS) to minimize the flow resistance loss of TF-MMCHS. The influence of different curved radii (r) on R_t , P_p , and S_{gen} of TC-MMCHS is investigated. The r values are set to 100, 125, 150, 175, and 200 μm , and TF-MMCHS is considered as the comparative object.

Fig. 10 The influence of different r values on R_t , P_p , and S_{gen}

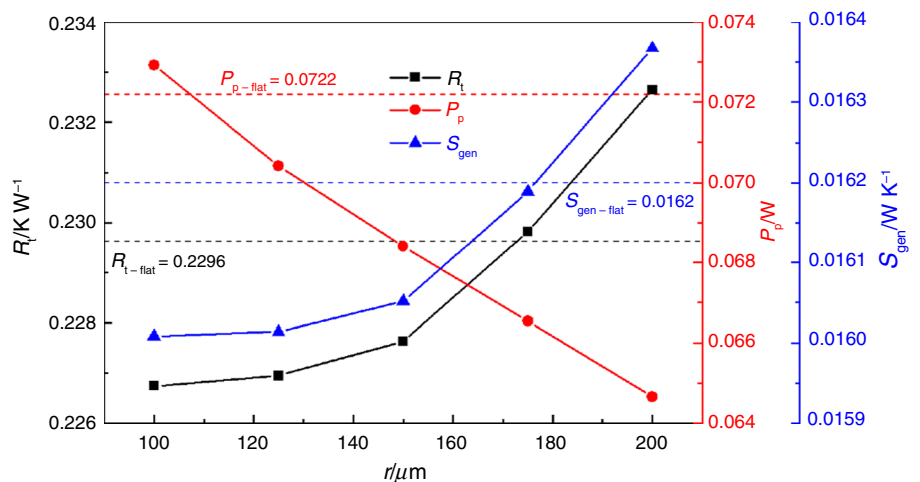


Figure 11a and b illustrates the velocity and streamline clouds of five different locations in TF-MMCHS and TC-MMCHS with $r=150 \mu m$, respectively. In general, the uniformity of the flow velocity of TC-MMCHS is obviously better than that of TF-MMCHS. It is well known that, when the nanofluid flows through the corner of TF-MMCHS, there is almost no coolant flowing through the lower half of the microchannel. This reduces its flow uniformity and results in increasing the flow resistance. The curved structure perfectly avoids this drawback. By comparing P2, P4, PB, and

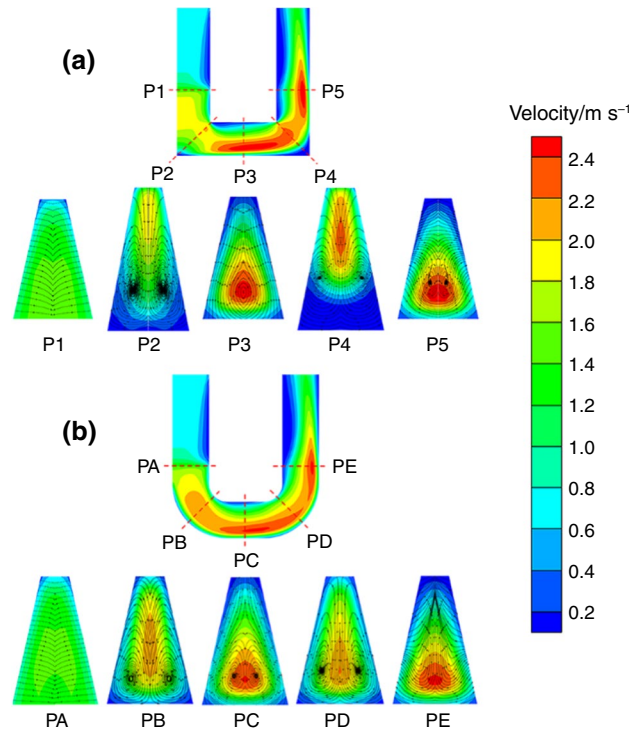


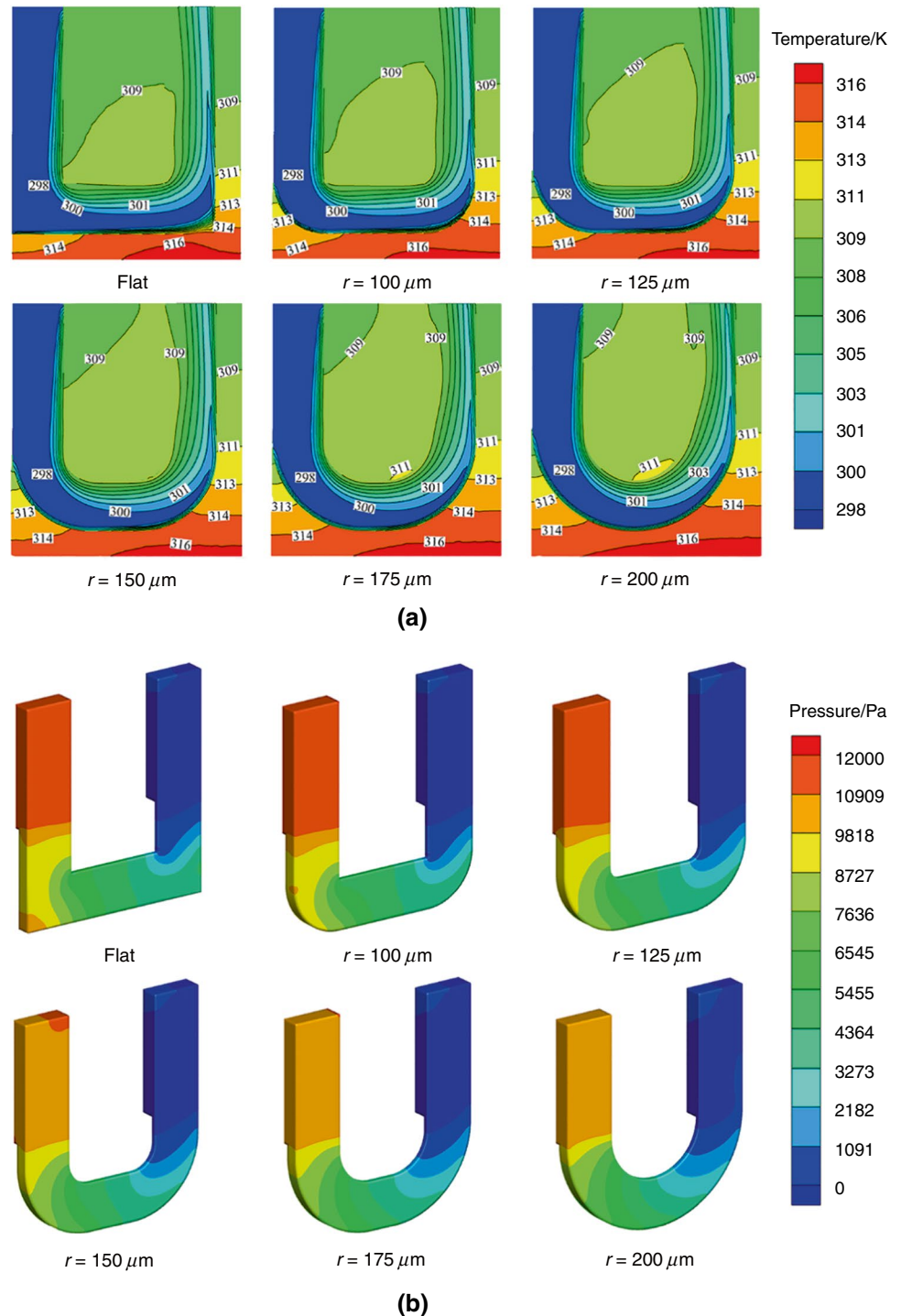
Fig. 11 The velocity and streamline clouds at different locations: a flat and b $r=150 \mu m$

PD, it can be deduced that the flow uniformity of the latter is significantly better than that of the former. Therefore, the curved structures at the channel corners have important role in reducing the flow resistance.

Figure 10 shows the effects of different r values. As r increases, R_t and S_{gen} also increase. It indicates that the cooling properties of TC-MMCHS gradually decrease and irreversible losses gradually grow. The dashed lines in

Fig. 10 represent the thermal resistance (R_{t-flat}), pumping power (P_{p-flat}), and entropy generation ($S_{gen-flat}$) of the TF-MMCHS. It can also be observed from Fig. 12a that, for $r < 175 \mu\text{m}$, the high-temperature area on the bottom of the heat sink becomes small, and the R_t value is less than 0.2296 K W^{-1} , which indicates a better heat transfer compared with that of TF-MMCHS. However, as r continues to increase, R_t becomes higher than R_{t-flat} , the

Fig. 12 a Temperature and b pressure contour maps of TC-MMCHS for different r values



high-temperature area becomes larger, and the temperature uniformity will deteriorate. This is because when r is small, the fluid disturbance at the turning point is more pronounced, which helps enhance the heat transfer in the corner regions to some extent. However, as r increases, the impact intensity decreases, and the flow disturbance reduces accordingly, leading to the reduction in cooling performance. Therefore, a smaller curved radii are more conducive to improving the heat transfer efficiency and cooling performance of TC-MMCHS.

As r increases, P_p shows a linear downward trend, decreasing by 11.33%, as illustrated in Fig. 10. The introduction of curved corners significantly reduces the pressure at the channel corner in TF-MMCHS (Fig. 12). In addition, when r increases, the magnitude of the pressure decrease tends to increase. When the coolant flows through the curved corner, the flow direction suddenly turns from longitudinal to transverse, and there will be a significant impact between the nanofluid and microchannel bottom, which leads to a significant pressure change in the TF-MMCHS [47]. The curved corner effectively mitigates the impact effect in the turn. Moreover, an increase in r value enhances the cushioning effect and reduces the pressure drop.

The trade-off between heat transfer performance as the cooling benefit and pump power consumption as the cooling cost has become an important factor in improving the comprehensive performance of TC-MMCHS. Therefore, it is necessary to comprehensively consider the impact of r on R_t and P_p . From Fig. 10, it can be observed that as r increases from 100 to 150 μm , R_t increases by 0.0009 K W^{-1} and P_p decreases by 0.0045 W K^{-1} , while as r increases from 150 to 200 μm , R_t increases by 0.0050 K W^{-1} and P_p decreases by 0.0038 W K^{-1} . The difference in the decrease of P_p between the two is relatively small, but the increase in R_t for the latter is 5.6 times higher than that of the former. Meanwhile, compared to TF-MMCHS, when $r = 150 \mu\text{m}$, the R_t and P_p of TC-MMCHS are smaller. Therefore, when $r = 150 \mu\text{m}$, the comprehensive performance of TC-MMCHS reaches the best.

Effect of the cross-section parameters of trapezoidal channel

To enhance the comprehensive performance of TC-MMCHS, the influence of structural parameters of the trapezoidal cross section is investigated. It mainly includes the bottom angle of the trapezoid (α) and the width of its central part (W_c), where $W_c = (W_a + W_b)/2$. Figure 13 shows the diagram of the structural parameters of the trapezoidal channel cross section.

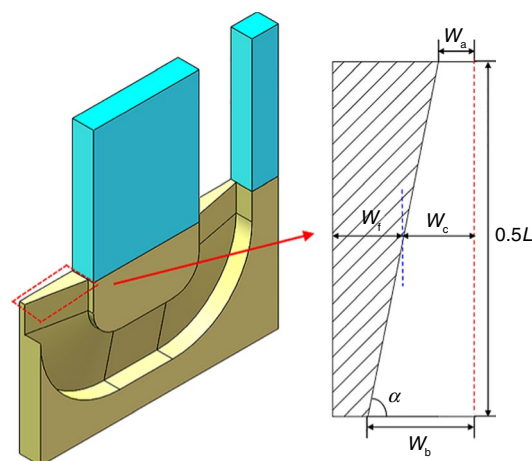


Fig. 13 Structural parameters diagram of the trapezoidal channel cross section

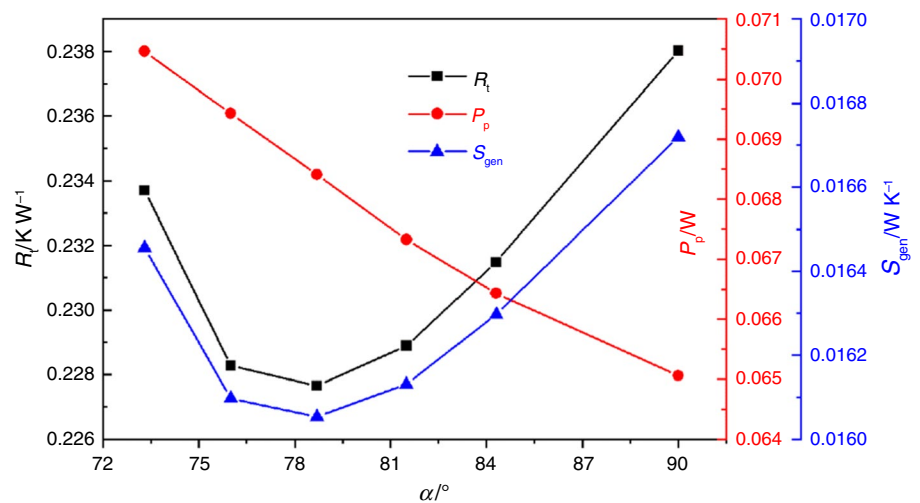
Effect of the bottom angle of trapezoid

W_c is set to 20 μm and α is varied by adjusting W_b . More precisely, α is set to 73.3, 76, 78.7, 81.5, 84.3, and 90° . Figure 14 illustrates the effect of different α values on R_t , P_p , and S_{gen} of TC-MMCHS.

When α increases, both R_t and S_{gen} of TC-MMCHS show a trend of first decreasing and then increasing. For $\alpha = 78.7^\circ$, both R_t and S_{gen} reach their minimum value, the heat transfer capacity reaches their optimum, and irreversible energy losses are minimized. It can be observed from Fig. 15 that for $\alpha = 73.3^\circ$ and $\alpha = 90^\circ$, there are significantly more high-temperature areas on the substrate, which results in poor heat transfer characteristics. When α is small, although the heat transfer region at the bottom of the trapezoidal channel increases, the larger width of channel leads to a lower flow rate, which suppresses the improvement of the heat transfer capacity. When α is large, the convective heat transfer area at the bottom of the microchannel decreases, and the high flow velocity region moves up, which is not conducive to increasing the cooling capacity of TC-MMCHS [20].

From Fig. 14, the increase of α has an improvement effect on P_p . However, the decrease effect is not significant, with a reduction of only 0.005 W. The fluid flow distribution provides a good explanation for the occurrence of this phenomenon. The high velocity zone is mainly concentrated in the lower part of the trapezoidal channel and forms two equal vortices, as shown in Fig. 15b. When α gradually increases, this region also gradually moves up and the vorticity gradually decreases. For $\alpha = 90^\circ$, it is a traditional rectangular channel. At this time, the vorticity in the channel is minimized, and the flow velocity distribution is relatively uniform, which reduces the flow resistance and minimizes the

Fig. 14 Effect of different α values on R_t , P_p , and S_{gen}



value of P_p . In practice, it must take into account both the cooling properties and required power consumption of TC-MMCHS. In this study, it is considered that the comprehensive performance of TC-MMCHS reaches its optimal state for $\alpha = 78.7^\circ$.

Effect of the trapezoidal channel width

The variation of the channel width is one of the significant factors influencing the overall performance of TC-MMCHS. The channel width (W_c) is set to 15, 17.5, 20, 22.5, and 25 μm , and α is set to 78.7° . Figure 16 shows the variation of R_t , P_p , and S_{gen} of TC-MMCHS for different W_c values.

When W_c increases, both R_t and S_{gen} show a gradually increasing trend. R_t increases from 0.209 to 0.256 W, which denotes an increase of 22.49%, while S_{gen} increases from 0.0151 to 0.0178 W K^{-1} , which represents an increase of 17.88%. It suggests that the increase of W_c is not conducive to improving the cooling properties of TC-MMCHS and reducing the irreversible energy losses. The increase of W_c improves the convective heat transfer area of the microchannel, at the expense of significantly reducing the flow rate of nanofluid, as shown in Fig. 17b. The high flow rate region in the lower part of the channel significantly decreases, which results in significantly reducing the convective heat transfer capacity, leading to the increase of R_t and S_{gen} [48].

Figure 16 demonstrates that increasing W_c significantly decreases P_p from 0.136 to 0.041 W, which denotes a decrease of 69.85%. The pressure contour maps illustrated in Fig. 17a clearly show that the pressure significantly drops with the increase of W_c . When W_c is small, the flow resistance becomes greater, which results in higher pressure loss. In addition, when W_c increases, the hydraulic diameter increases and high flow velocity area gradually decreases,

which effectively reduces the pressure drop. This is consistent with the results obtained by Yang et al. [49].

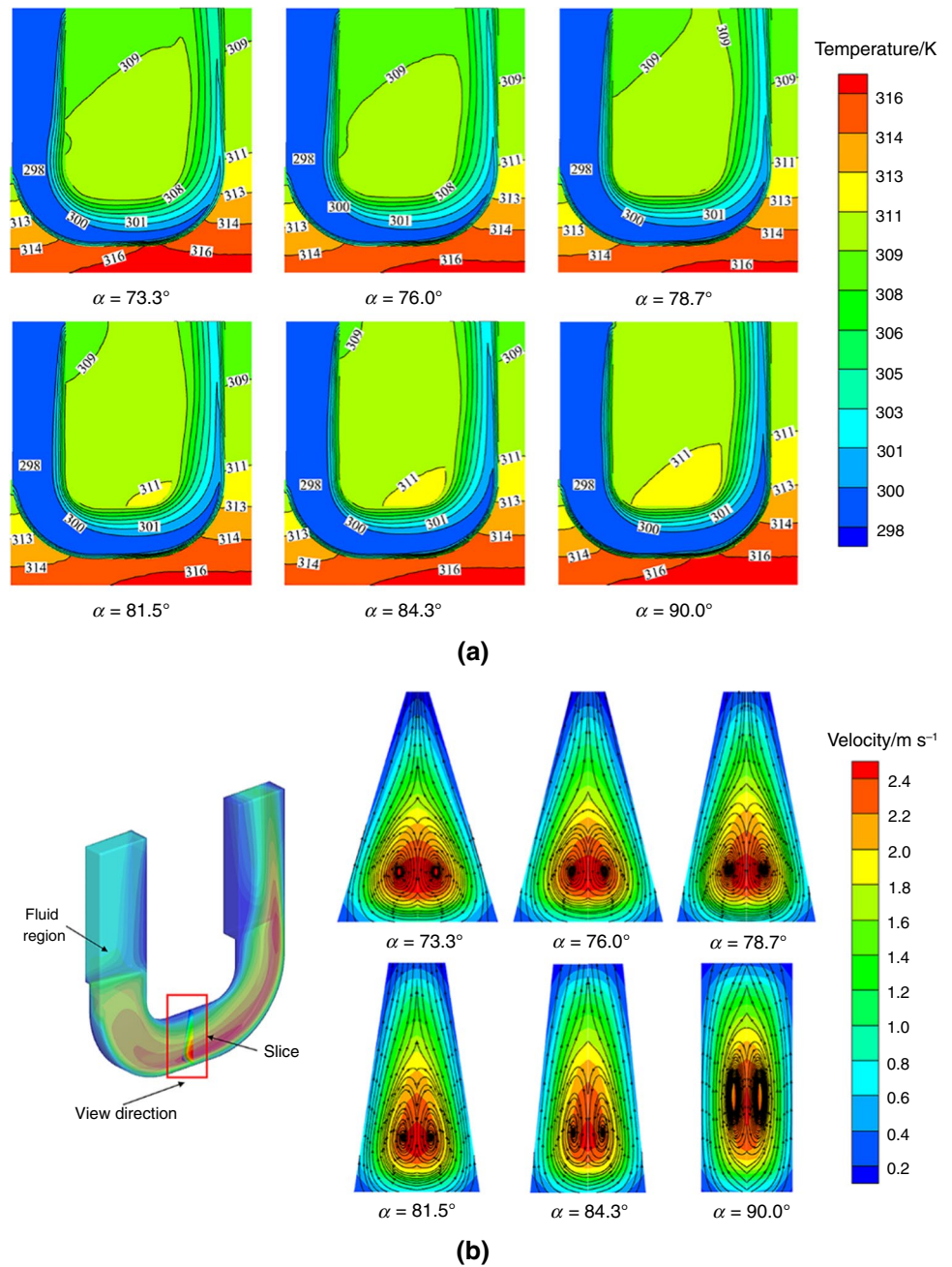
In order to further improve the overall performance of TC-MMCHS, the interaction effects of the structural parameters of the trapezoidal cross section on the R_t , P_p , and S_{gen} of TC-MMCHS are investigated. Combining Figs. 14 and 16, both R_t and S_{gen} exhibit the same trend of variation, regardless of the changes in α or W_c . The maximum changes in R_t and S_{gen} caused by the variation in α are 0.010 K W^{-1} and 0.0007 W K^{-1} , respectively. As W_c increases, the changes in R_t and S_{gen} can reach 0.047 K W^{-1} and 0.0028 W K^{-1} , respectively. Therefore, the variation of R_t and S_{gen} of TC-MMCHS is mainly influenced by W_c . When $\alpha = 78.8^\circ$ and $W_c = 15 \mu\text{m}$, the values of R_t and S_{gen} of TC-MMCHS are the smallest, with the best heat transfer performance and the smallest irreversible losses. At the same time, it can also be observed that the change in W_c has a much greater impact on P_p than α , and the change in W_c is the dominant factor in the pressure drop change of TC-MMCHS. As α and W_c increase, the values of P_p show gradually decreasing trend. When both α and W_c are maximum ($\alpha = 90^\circ$, $W_c = 25 \mu\text{m}$), TC-MMCHS has the smallest P_p and the lowest energy consumption.

Effect of the nanoparticle volume fraction

The influence of the volume fraction of Al_2O_3 -water nanofluid (φ) on R_t , P_p , and S_{gen} of TC-MMCHS is studied. The values of φ are set to 0 (deionized water), 1, 2, 3, and 4%.

Figure 18 shows the variation of R_t , P_p , and S_{gen} at different φ values. It shows that Al_2O_3 -water nanofluid remarkably improves the cooling characteristics of TC-MMCHS compared with deionized water ($\varphi = 0$). In addition, the increase of φ results in gradually increasing the heat transfer capacity, while R_t decreases by 4.13, 8.94, 12.43, and 16.32%. Moreover, the increase of φ reduces the maximum temperature of heat sink surface and significantly improves

Fig. 15 **a** Temperature and **b** velocity contour maps in the middle cross section of the channel for different α values

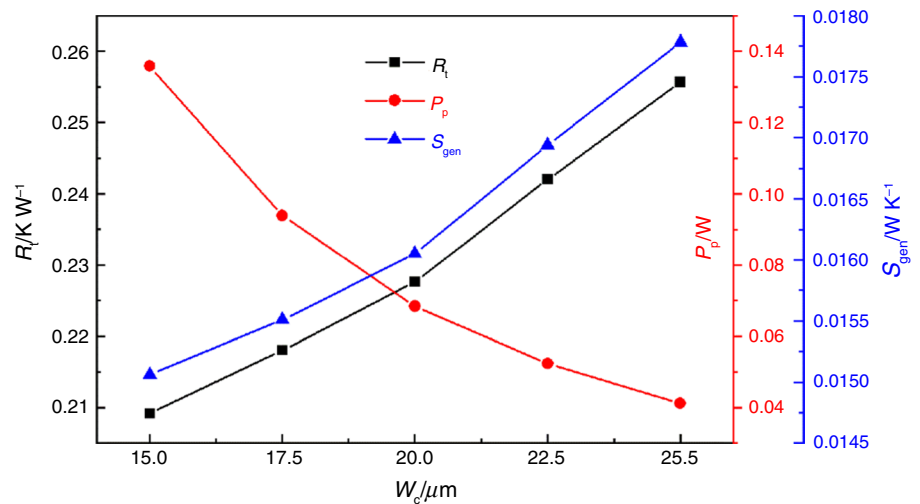


its temperature uniformity, as illustrated in Fig. 19. This is primarily because the introduction of Al_2O_3 suspended particles improves the heat conductivity, compared with deionized water. When φ increases, the number of nanoparticles also increases, which results in enhancing the interaction

between coolant and microchannel wall, leading to a prominent improvement in the cooling performance [50].

Although the increase of φ favors the cooling performance of TC-MMCHS, the corresponding additional power consumption increases. From Fig. 18, when φ

Fig. 16 The influence of different W_c values on R_t , P_p , and S_{gen}



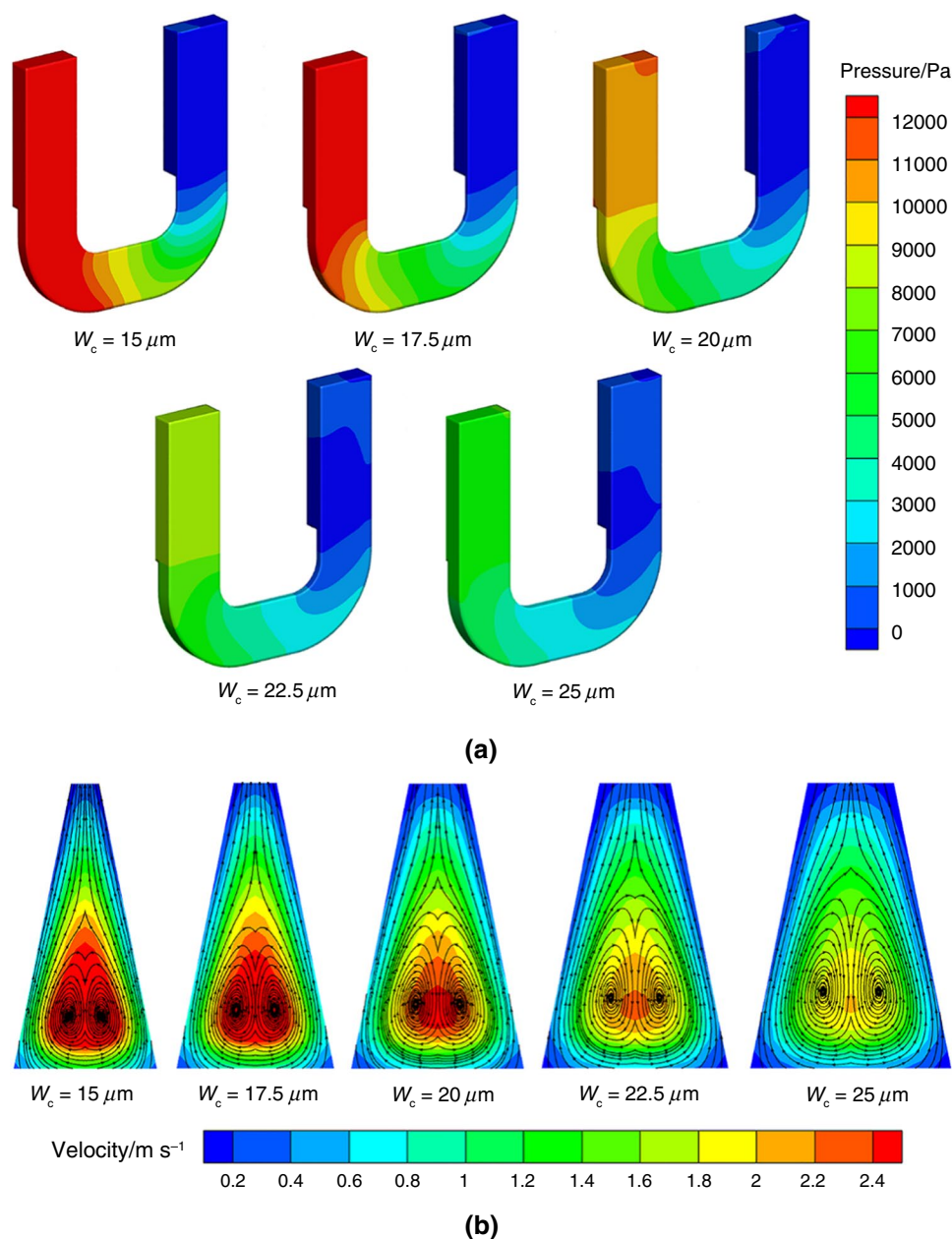
increases, P_p linearly increases. This is because the increase of φ makes the nanofluid more viscous, and the flow resistance grows, which results in increasing the power consumption of the heat exchange system. Therefore, when choosing a suitable φ value, the effects of the power consumption and thermal properties should be considered. In addition, the increase of φ results in a decrease of S_{gen} by 13.45%, which indicates a decrease in the irreversible losses of the system. In this study, the magnitude order of the heat transfer entropy generation is much higher than that of the friction entropy generation, and it takes a dominant role in the S_{gen} [10]. Therefore, the variation trend (gradually decreasing) of S_{gen} is consistent with that of R_t .

Conclusions

In order to improve the flow and heat transfer characteristics of the conventional MMCHS, this paper proposes a novel MMCHS combining trapezoidal cross-section and curved corners and using the Al_2O_3 -water nanofluid as the coolant. The superiority of different channel cross-section shapes is discussed, and the effects of r , α , W_c , and φ of the TC-MMCHS are studied. The main findings are as follows:

- (1) For the same Re , R_t and S_{gen} of F-MMCHSs with four different structures always exhibit the following pattern in descending order: TF-MMCHS, HEF-MMCHS, RF-MMCHS, and ITF-MMCHS. For the same P_p , the R_t

Fig. 17 **a** Pressure contours and **b** velocity contours for different W_c values



and S_{gen} of TF-MMCHS are the smallest, exhibiting the highest overall performance.

- (2) The introduction of curved corners decreases the flow resistance of TF-MMCHS and enhances its cooling capacity. For $Re = 60$, the P_p of TC-MMCHS decreases by up to 11.33%, compared with that of TF-MMCHS.
- (3) The structural parameters of trapezoidal channel have different degrees of influence on TC-MMCHS performance. When α increases, R_t and S_{gen} exhibit a trend of first decreasing and then increasing. For $\alpha = 78.7^\circ$, the heat transfer properties and irreversible losses reach their optimal level. The increase of W_c is not beneficial

to improving cooling performance. However, it significantly reduces P_p (by up to 69.85%).

- (4) The Al_2O_3 –water nanofluid enhances the cooling performance and reduces the irreversible losses in TC-MMCHS, compared with deionized water ($\varphi = 0$). When φ increases, R_t and S_{gen} , respectively, decrease by 16.32% and 13.45%, at the expense of increasing P_p . Therefore, φ should not have a very large value, and it should be optimized based on evaluation indicators.
- (5) This nanofluid with low particle concentration and small particle size is selected in this study to ensure its low deposition rate and avoid blocking microchan-

Fig. 18 Effect of ϕ on the R_t , P_p , and S_{gen} of TC-MMCHS

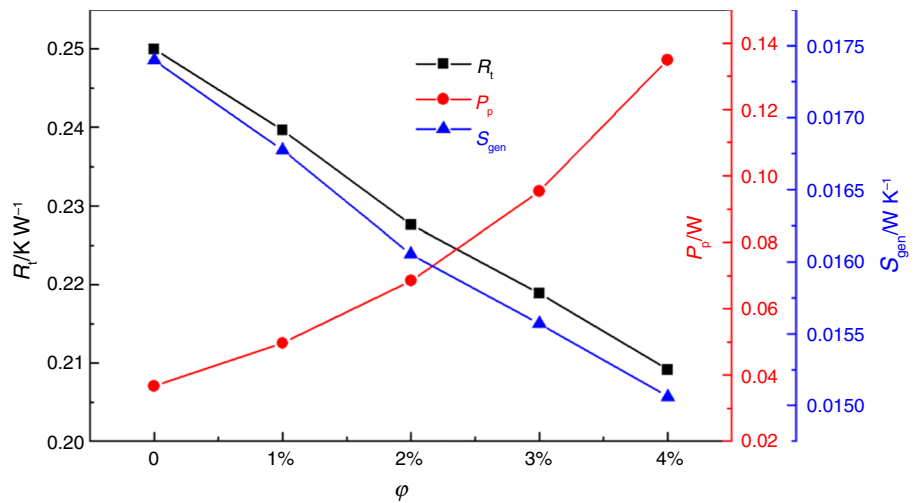
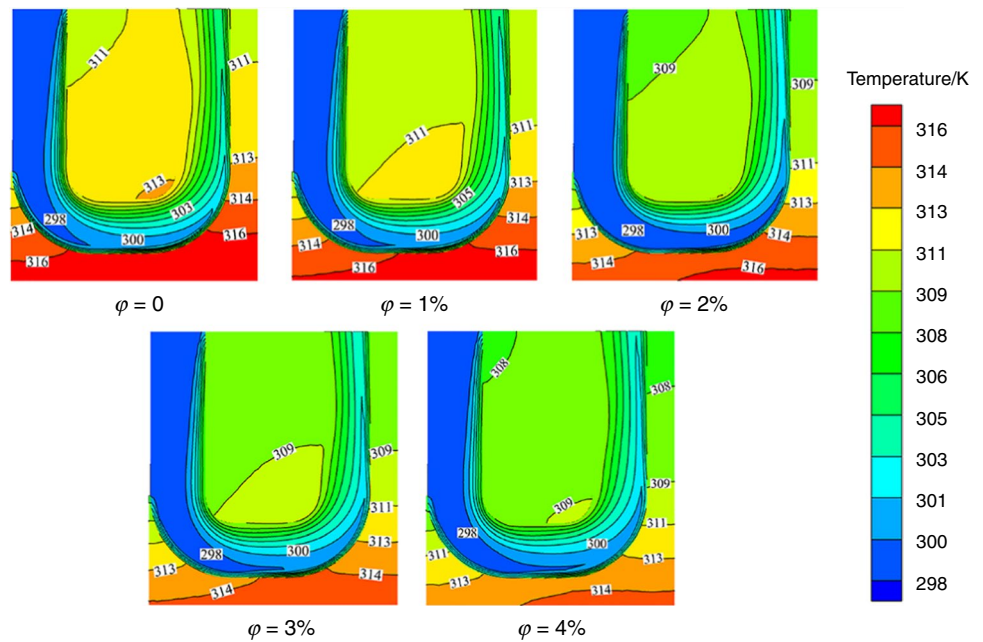


Fig. 19 Temperature contour maps of TC-MMCHS for different ϕ values



nels. To improve the flow and heat transfer stability of nanofluids, adding surfactants to nanofluids can be considered in subsequent research. Meanwhile, considering the practical processing issues, the current advanced manufacturing technology (e.g., 3D printing) can be utilized to provide suitable processing methods for the heat sink.

Acknowledgements This work was financially supported by the National Natural Science Foundation of China (No.52306194) and Anhui Provincial Natural Science Foundation (No.2308085ME176).

Author contributions Zhiguo Tang performed conceptualization, methodology, investigation, formal analysis, and writing—original draft. Ran Sun performed data curation, writing—original draft, and

reviewing manuscript. Kuan Lu provided investigation and validation. Jianping Cheng approved investigation, supervision resources, and methodology. Pei Zhou conducted validation and reviewing manuscript.

Data availability No data were used for the research described in the article.

Declarations

Conflict of interest The authors declare that they have no known competing financial interests or personal relationships that could have appeared to influence the work reported in this paper.

References

- Deng D, Zeng L, Sun W. A review on flow boiling enhancement and fabrication of enhanced microchannels of microchannel heat sinks. *Int J Heat Mass Transf.* 2021;175:121332. <https://doi.org/10.1016/j.ijheatmasstransfer.2021.121332>.
- Zhang X, Ji Z, Wang J, Lv X. Research progress on structural optimization design of microchannel heat sinks applied to electronic devices. *Appl Therm Eng.* 2023;235:121294. <https://doi.org/10.1016/j.applthermaleng.2023.121294>.
- Sefiane K, Koşar A. Prospects of heat transfer approaches to dissipate high heat fluxes: opportunities and challenges. *Appl Therm Eng.* 2022;215:118990. <https://doi.org/10.1016/j.applthermaleng.2022.118990>.
- Zhang Z, Cui H, Zhao S, Zhao R, Wu T, Liu Z, Liu W. Simulation of heat and mass transfer process in a flat-plate loop heat pipe and experimental comparison. *Appl Therm Eng.* 2023;220:119705. <https://doi.org/10.1016/j.applthermaleng.2022.119705>.
- Zhang D, Qu H, Lan J, Chen J, Xie Y. Flow and heat transfer characteristics of single jet impinging on protrusioned surface. *Int J Heat Mass Transf.* 2013;58(1–2):18–28. <https://doi.org/10.1016/j.ijheatmasstransfer.2012.11.019>.
- Tan L, Zhang J, Xu H. Jet impingement on a rib-roughened wall inside semi-confined channel. *Int J Therm Sci.* 2014;86:210–8. <https://doi.org/10.1016/j.ijthermalsci.2014.06.037>.
- Pan Y, Zhao R, Nian Y, Cheng W. Study on the flow and heat transfer characteristics of pin-fin manifold microchannel heat sink. *Int J Heat Mass Transf.* 2022;183:122052. <https://doi.org/10.1016/j.ijheatmasstransfer.2021.122052>.
- Cui P, Liu Z. Experimental study on flow boiling in ultrahigh-aspect-ratio copper microchannel heat sink. *Appl Therm Eng.* 2023;223:119975. <https://doi.org/10.1016/j.applthermaleng.2023.119975>.
- Sharma JP, Sharma A, Jilte RD, Kumar R, Ahmadi MH. A study on thermohydraulic characteristics of fluid flow through microchannels. *J Therm Anal Calorim.* 2020;140:1–32. <https://doi.org/10.1007/s10973-019-08741-4>.
- Ma Z, Hu C, Ma L, Chen H, Hou J, Hao N, Wei J. Nanofluids in microchannel heat sinks for efficient flow cooling of power electronic devices. *Appl Mater Today.* 2023;35:101980. <https://doi.org/10.1016/j.apmt.2023.101980>.
- Tuckerman DB, Pease RFW. High-performance heat sinking for VLSI. *IEEE Electron Device Lett.* 1981;2(5):126–9. <https://doi.org/10.1109/EDL.1981.25367>.
- Khodabandeh E, Rozati SA, Joshaghani M, Akbari OA, Akbari S, Toghraie D. Thermal performance improvement in water nanofluid/GNP–SDBS in novel design of double-layer microchannel heat sink with sinusoidal cavities and rectangular ribs. *J Therm Anal Calorim.* 2019;136:1333–45. <https://doi.org/10.1007/s10973-018-7826-2>.
- Zhai YL, Xia GD, Liu XF, Li YF. Heat transfer in the microchannels with fan-shaped reentrant cavities and different ribs based on field synergy principle and entropy generation analysis. *Int J Heat Mass Transf.* 2014;68:224–33. <https://doi.org/10.1016/j.ijheatmasstransfer.2013.08.086>.
- Zhu Q, Jin Y, Chen J, Su R, Zhu F, Li H, Wan J, Zhang H, Sun H, Cui Y, Xia H. Computational study of rib shape and configuration for heat transfer and fluid flow characteristics of microchannel heat sinks with fan-shaped cavities. *Appl Therm Eng.* 2021;195:117171. <https://doi.org/10.1016/j.applthermaleng.2021.117171>.
- Sikdar P, Datta A, Biswas N, Sanyal D. Identifying improved microchannel configuration with triangular cavities and different rib structures through evaluation of thermal performance and entropy generation number. *Phys Fluids.* 2020;32(3):033601. <https://doi.org/10.1063/1.5137842>.
- Raja Kuppasamy N, Saidur R, Ghazali NNN, Mohammed HA. Numerical study of thermal enhancement in micro channel heat sink with secondary flow. *Int J Heat Mass Transf.* 2014;78:216–23. <https://doi.org/10.1016/j.ijheatmasstransfer.2014.06.072>.
- Ghani IA, Sidik NAC, Mamat R, Najafi G, Ken TL, Asako Y, Japar WMAA. Heat transfer enhancement in microchannel heat sink using hybrid technique of ribs and secondary channels. *Int J Heat Mass Transf.* 2017;114:640–55. <https://doi.org/10.1016/j.ijheatmasstransfer.2017.06.103>.
- Zhu J, Li X, Wang S, Yang Y, Wang X. Performance comparison of wavy microchannel heat sinks with wavy bottom rib and side rib designs. *Int J Therm Sci.* 2019;146:106068. <https://doi.org/10.1016/j.ijthermalsci.2019.106068>.
- Wang S, Zhu J, An D, Zhang B, Chen L, Yang Y, Zheng S, Wang X. Heat transfer enhancement of symmetric and parallel wavy microchannel heat sinks with secondary branch design. *Int J Therm Sci.* 2022;171:107229. <https://doi.org/10.1016/j.ijthermalsci.2021.107229>.
- Zhang Y, Wang S, Ding P. Effects of channel shape on the cooling performance of hybrid micro-channel and slot-jet module. *Int J Heat Mass Transf.* 2017;113:295–309. <https://doi.org/10.1016/j.ijheatmasstransfer.2017.05.092>.
- Gunnasegaran P, Mohammed HA, Shuaib NH, Saidur R. The effect of geometrical parameters on heat transfer characteristics of microchannels heat sink with different shapes. *Int Commun Heat Mass Transf.* 2010;37:1078–86. <https://doi.org/10.1016/j.icheatmasstransfer.2010.06.014>.
- Harpole GM, Eninger JE. Micro-channel heat exchanger optimization. *IEEE Semicond Therm Meas Manag Symp.* 2002. <https://doi.org/10.1109/STHERM.1991.152913>.
- Luo Y, Zhang J, Li W. A comparative numerical study on two-phase boiling fluid flow and heat transfer in the microchannel heat sink with different manifold arrangements. *Int J Heat Mass Transf.* 2020;156:119864. <https://doi.org/10.1016/j.ijheatmasstransfer.2020.119864>.
- Lin Y, Luo Y, Li W, Cao Y, Tao Z, Shih TI. Single-phase and two-phase flow and heat transfer in microchannel heat sink with various manifold arrangements. *Int J Heat Mass Transf.* 2021;171:121118. <https://doi.org/10.1016/j.ijheatmasstransfer.2021.121118>.
- Chen C, Wang X, Yuan B, Du W, Xin G. Investigation of flow and heat transfer performance of the manifold microchannel with different manifold arrangements. *Case Stud Therm Eng.* 2022;34:102073. <https://doi.org/10.1016/j.csite.2022.102073>.
- Mandel R, Shoostari A, Ohadi M. A “2.5-D” modeling approach for single-phase flow and heat transfer in manifold microchannels. *Int J Heat Mass Transf.* 2018;126:317–30. <https://doi.org/10.1016/j.ijheatmasstransfer.2018.04.145>.
- Gilmore N, Timchenko V, Menictas C. Open manifold microchannel heat sink for high heat flux electronic cooling with a reduced pressure drop. *Int J Heat Mass Transf.* 2020;163:120395. <https://doi.org/10.1016/j.ijheatmasstransfer.2020.120395>.
- Tang K, Lin G, Guo Y, Huang J, Zhang H, Miao J. Simulation and optimization of thermal performance in diverging/converging manifold microchannel heat sink. *Int J Heat Mass Transf.* 2023;200:123495. <https://doi.org/10.1016/j.ijheatmasstransfer.2022.123495>.
- Cheng J, Xu H, Tang Z, Zhou P. Multi-objective optimization of manifold microchannel heat sink with corrugated bottom impacted by nanofluid jet. *Int J Heat Mass Transf.* 2023;201:123634. <https://doi.org/10.1016/j.ijheatmasstransfer.2022.123634>.
- Deymi-Dashtebayaz M, Akhouni M, Ebrahimi-Moghadam A, Arabkoohsar A, Jabari Moghadam A, Farzaneh-Gord M. Thermohydraulic analysis and optimization of Cu/water nanofluid

- inside helically dimpled heat exchangers. *J Therm Anal Calorim.* 2021;143:4009–24. <https://doi.org/10.1007/s10973-020-09398-0>.
31. Nazari M, Karami M, Ashouri M. Comparing the thermal performance of water, ethylene glycol, alumina and CNT nanofluids in CPU cooling: experimental study. *Exp Therm Fluid Sci.* 2014;57:371–7. <https://doi.org/10.1016/j.expthermflusci.2014.06.003>.
 32. Ahammed N, Asirvatham LG, Wongwises S. Thermoelectric cooling of electronic devices with nanofluid in a multiport minichannel heat exchanger. *Exp Therm Fluid Sci.* 2016;74:81–90. <https://doi.org/10.1016/j.expthermflusci.2015.11.023>.
 33. Afshari F, Tuncer AD, Sözen A, Variyenli HI, Khanlari A, Gürbüz EY. A comprehensive survey on utilization of hybrid nanofluid in plate heat exchanger with various number of plates. *Int J Num Methods Heat Fluid Flow.* 2022;32:241–64. <https://doi.org/10.1108/HFF-11-2020-0743>.
 34. Yue Y, Mohammadian SK, Zhang Y. Analysis of performances of a manifold microchannel heat sink with nanofluids. *Int J Therm Sci.* 2015;89:305–13. <https://doi.org/10.1016/j.ijthermalsci.2014.11.016>.
 35. Alfaryjat AA, Mohammed HA, Adam NM, Stanciu D, Dobrovicescu A. Numerical investigation of heat transfer enhancement using various nanofluids in hexagonal microchannel heat sink. *Therm Sci Eng Prog.* 2018;5:252–62. <https://doi.org/10.1016/j.tsep.2017.12.003>.
 36. Pourfattah F, Abbasian Arani AA, Babaie MR, Nguyen HM, Asadi A. On the thermal characteristics of a manifold microchannel heat sink subjected to nanofluid using two-phase flow simulation. *Int J Heat Mass Transf.* 2019;143:118518. <https://doi.org/10.1016/j.ijheatmasstransfer.2019.118518>.
 37. Sabaghan A, Edalatpour M, Moghadam MC, Roohi E, Niazmand H. Nanofluid flow and heat transfer in a microchannel with longitudinal vortex generators: two-phase numerical simulation. *Appl Therm Eng.* 2016;100:179–89. <https://doi.org/10.1016/j.applthermaleng.2016.02.020>.
 38. Pop I, Grosan T, Revnic C, Roşca AV. Unsteady flow and heat transfer of nanofluids, hybrid nanofluids, micropolar fluids and porous media: a review. *Therm Sci Eng Prog.* 2023;46:102248. <https://doi.org/10.1016/j.tsep.2023.102248>.
 39. Yin Y, Shangguan X, Ma X, Zhang J, Qin Y. Influence of corner structure of fuel cell serpentine channel on water removal. *Int J Hydrog Energ.* 2020;45(54):29812–23. <https://doi.org/10.1016/j.ijhydene.2019.08.200>.
 40. Hou Y, Zhang G, Qin Y, Du Q, Jiao K. Numerical simulation of gas liquid two-phase flow in anode channel of low-temperature fuel cells. *Int J Hydrog Energ.* 2017;42(5):3250–8. <https://doi.org/10.1016/j.ijhydene.2016.09.219>.
 41. Azman A, Mukhtar A, Yusoff MZ, Gunnasegaran P, Khai Ching N, Md Yasir ASH. Numerical investigation of flow characteristics and heat transfer efficiency in sawtooth corrugated pipes with Al₂O₃-CuO/Water hybrid nanofluid. *Results Phys.* 2023;53:106974. <https://doi.org/10.1016/j.rinp.2023.106974>.
 42. Garoosi F. Presenting two new empirical models for calculating the effective dynamic viscosity and thermal conductivity of nanofluids. *Powder Technol.* 2020;366:788–820. <https://doi.org/10.1016/j.powtec.2020.03.032>.
 43. Chai L, Wang L. Thermal-hydraulic performance of interrupted microchannel heat sinks with different rib geometries in transverse microchambers. *Int J Therm Sci.* 2018;127:201–12. <https://doi.org/10.1016/j.ijthermalsci.2018.01.029>.
 44. Drummond KP, Back D, Sinanis MD, Janes DB, Peroulis D, Weibel JA, Garimella SV. A hierarchical manifold microchannel heat sink array for high-heat-flux two-phase cooling of electronics. *Int J Heat Mass Transf.* 2018;117:319–30. <https://doi.org/10.1016/j.ijheatmasstransfer.2017.10.015>.
 45. Kose HA, Yildizeli A, Cadirci S. Parametric study and optimization of microchannel heat sinks with various shapes. *Appl Therm Eng.* 2022;211:118368. <https://doi.org/10.1016/j.applthermaleng.2022.118368>.
 46. Dai H, Liu Y. Entropy generation analysis on thermo-hydraulic characteristics of microencapsulated phase change slurry in wavy microchannel with porous fins. *Appl Therm Eng.* 2023;219:119440. <https://doi.org/10.1016/j.applthermaleng.2022.119440>.
 47. Shi D, Jing Q, Gao T, Zhang D, Xie Y. Flow and heat transfer mechanism of U-shaped channel considering variable cross-section and rotating effects. *Int Commun Heat Mass Transf.* 2021;129:105701. <https://doi.org/10.1016/j.icheatmasstransfer.2021.105701>.
 48. Wang Z, Li M, Ren F, Ma B, Yang H, Zhu Y. Sobol sensitivity analysis and multi-objective optimization of manifold microchannel heat sink considering entropy generation minimization. *Int J Heat Mass Transf.* 2023;208:124046. <https://doi.org/10.1016/j.ijheatmasstransfer.2023.124046>.
 49. Yang J, Cheng K, Zhang K, Huang C, Huai X. Numerical study on thermal and hydraulic performances of a hybrid manifold microchannel with bifurcations for electronics cooling. *Appl Therm Eng.* 2023;232:121099. <https://doi.org/10.1016/j.applthermaleng.2023.121099>.
 50. Lv J, Chang S, Hu C, Bai M, Wang P, Zeng K. Experimental investigation of free single jet impingement using Al₂O₃-water nanofluid. *Int Commun Heat Mass Transf.* 2017;88:126–35. <https://doi.org/10.1016/j.icheatmasstransfer.2017.08.017>.

Publisher's Note Springer Nature remains neutral with regard to jurisdictional claims in published maps and institutional affiliations.

Springer Nature or its licensor (e.g. a society or other partner) holds exclusive rights to this article under a publishing agreement with the author(s) or other rightsholder(s); author self-archiving of the accepted manuscript version of this article is solely governed by the terms of such publishing agreement and applicable law.